



1 Predicting tidal heights for extreme environments: From 25 h 2 observations to accurate predictions at Jang Bogo Antarctic Research 3 Station, Ross Sea, Antarctica

4 Do-Seong Byun¹, Deirdre E. Hart²

5 ¹Ocean Research Division, Korea Hydrographic and Oceanographic Agency, Busan 49111, Republic of Korea

6 ²School of Earth and Environment, University of Canterbury, Christchurch 8140, Aotearoa New Zealand

7 Correspondence to: Do-Seong Byun (dsbyun@korea.kr)

8 **Abstract.** Accurate tidal height data for the seas around Antarctica are much needed, given the crucial role of tidal processes
9 as represented in regional and global climate, ocean and marine cryosphere models. Though obtaining long term sea level
10 records for traditional tidal predictions is extremely difficult around ice affected coasts. This study evaluates the ability of a
11 relatively new, tidal species based approach, the Complete Tidal Species Modulation with Tidal Constant Corrections
12 (CTSM+TCC) method, to accurately predict tides for a temporary tidal station in the Ross Sea, Antarctica using records from
13 a nearby reference station characterized by a different regime. Predictions for the ‘mixed, mainly diurnal’ regimes of Jang
14 Bogo Antarctic Research Station (JBARS) were made and evaluated based on summertime (2017; and 2018 to 2019) short-
15 term (25 h) observations at this temporary station, along with tidal prediction data derived from yearlong observations (2013)
16 from the nearby, ‘diurnal’ regime of Cape Roberts (ROBT). Results reveal the CTSM+TCC method can produce accurate (to
17 within ~5 cm Root Mean Square Errors) tidal predictions for JBARS when using short-term (25 h) tidal data from periods with
18 higher than average tidal ranges (i.e. tropic-spring periods). Predictions were successful due to the similar relationships
19 between the main tidal constituents’ (K_1 and O_1 tides) phase-lag differences at the prediction and reference stations, and despite
20 these tidal stations being characterized by different tidal regimes according to their form factors (i.e. mixed, mainly diurnal
21 versus diurnal). We demonstrate how to determine optimal short-term data collection periods based on the Moon’s declination.
22 The importance of using long period tides to improve tidal prediction accuracy is also considered, along with the characteristics
23 of the different decadal scale tidal variations around Antarctica, from the four major FES2014 tidal harmonic constants.

24

25 1 Introduction

26 Conventionally, yearlong sea level records are used to generate accurate tidal height predictions via harmonic methods (e.g.
27 Codiga, 2011; Foreman, 1977; Pawlowicz et al. 2002). Obtaining long term records for such tidal analyses is extremely difficult
28 for sea ice affected coasts, like that surrounding Antarctica (Rignot et al. 2000). However, Byun and Hart (2015) developed a
29 new approach to successfully predict tidal heights based on as little as ≥ 25 h of sea level records, combined with nearby
30 reference site records, using their Complete Tidal Species Modulation with Tidal Constant Corrections (CTSM+TCC) method,
31 on the coasts of Korea and New Zealand. Demonstrating the usefulness of this method for generating accurate tidal predictions
32 for new sites on sea ice affected coasts is the motivation for this study. We focus on the Ross Sea, Antarctica, as our case study
33 area.

34 Long-term, quality sea level records in the Ross Sea are few and far between, and include observations from gauges operated
35 by New Zealand at Cape Roberts (ROBT); by the United States in McMurdo Sound; and by Italy at Mario Zucchelli Station,
36 all in eastern Terra Nova Bay. Permanent sea level gauge installations in this extreme environment must accommodate or
37 somehow avoid surface vents freezing over with sea ice, as well as damage to subsurface instruments from icebergs. At ROBT,



these issues have been avoided by sheltering the sea level sensor towards the bottom of a 10 m long hole, drilled through a large shore boulder, from its surface ~2 m above the sea and sea ice level, to ~6 m below sea level below the base of the sea ice (Glen Rowe, Technical Leader Sea Level Data, New Zealand Hydrographic Authority, *pers. comm.* 13 Dec. 2019). In the absence of a suitable permanent gauge site, such as the current situation at the Korean Jang Bogo Antarctic Research Station (JBARS), hydrographic surveys are best conducted during the summertime predominantly sea ice free window around mid-January to mid-February. Even then, mobile ice (Figure 1) and severe weather events frequently hinder such surveys via instrument damage or loss, not to mention the logistical difficulties of instrument deployment and recovery (Rignot et al. 2000). Accurate tidal records from the Ross Sea and other areas around Antarctica are thus scarce compared to those available from other regions, though these data are much needed given the crucial role of tidal processes around this continent (Han and Lee, 2018; Han et al., 2005; Jourdain et al., 2018; Padman et al., 2002; 2003; 2008; 2018).

Floating ice shelves occupy around 75% of Antarctica's perimeter (Padman et al., 2018). Tidal oscillations at the ice-ocean interface influence the location and extent of grounding zones (Padman et al., 2002; Rosier and Gudmundsson, 2018), and control heat transfers and ocean mixing in cavities beneath the marine cryosphere (Padman et al., 2018; Wild et al., 2019) and the calving and subsequent drift of icebergs (Rignot et al. 2000). Tides also affect variability in polynyas; patterns of seasonal sea ice; and thus the functioning of marine ecosystems (Han and Lee, 2018). In addition, tides affect the dynamics of landfast sea ice, which provides aircraft landing zones for Antarctic science operations (Han and Lee, 2018).

Accurate Antarctic region tidal input data are needed for models examining changes in global climate and ocean circulation, including for the generation of Antarctic bottom water (Han and Lee, 2018; Wild et al., 2019). Data on coastal tides are also essential for studies of ice mass balances and motions (Han and Lee, 2018; Padman et al., 2008; 2018; Rignot et al. 2000; Rosier and Gudmundsson, 2018; Wild et al., 2019). Ice thickness is typically measured via the subtraction of tidal height oscillations from highly accurate, but relatively low frequency, satellite imagery based observations of ice surface elevation and/or from in situ Global Positioning System (GPS) instrument observations (Padman et al., 2008). For floating ice, this procedure is relatively straightforward but where ice shelves and glacier tongues occur, the mechanics of grounding zones and ice flexure render the determination of ice thickness and motion very challenging (Padman et al. 2018; Rosier and Gudmundsson, 2018), making the accuracy of the tidal height inputs crucial for effective ice modelling (Wild et al. 2019).

In this study, we tested applicability of Byun and Hart's (2015) CTSM+TCC method in an extreme observation environment using 25 h short-term records from JBARS, our temporary tidal observation station, and yearlong data from ROBT, the nearby reference station. Sect. 2 of this paper details the JBARS and ROBT observation data sets used to generate harmonic tidal analysis results and CTSM+TCC tidal predictions. Sect. 3 explains the CTSM+TCC method and settings, while Section 4 demonstrates the CTSM+TCC tidal prediction capability. Sect. 5 discusses the generation of double tidal peaks, particularly during low tides, and tidal characteristics around Antarctica.

2 Antarctica's major tides: Observations and background

2.1 Study sites and data records

The Korea Hydrographic and Oceanographic Agency (KHOA) survey team went to JBARS in Northern Victoria Land's Terra Nova Bay, Ross Sea, Antarctica, in the summertime of 2017 (Figure 2) for a preliminary fieldtrip to conduct hydrographic surveys and produce a nautical chart. This mission collected the first 19 day sea level records for JBARS: 10 min interval observation data were recorded from 29 January to 16 February 2017 using a bottom-mounted pressure sensor (WTG-256S AAT, Korea). High frequency signals were removed from the observation record using a fifth-order low-pass Butterworth filter, with a cut-off frequency of 3 h. We use these data in our study's tidal prediction experiments as the temporary tidal station's primary observation record.



78 For the purposes of a full-scale survey, 3 additional, discontinuous sea level observation records were measured by KHOA at
79 JBARS between 29 December 2018 and 11 March 2019, all at 10 min intervals using the same type of instrument. Of these,
80 the 20.54 day record produced between 29 December 2018 and 18 January 2019 comprised relatively high quality data with
81 small residuals. We used this additional dataset to verify the CTSM+TCC method tidal predictions generated from input
82 parameters derived from daily (25 h) slices of the 2017 sea level records. Due to the short duration of the KHOA survey team's
83 2017 and 2018 to 2019 forays into the Ross Sea, and the absence of in situ instruments, it was not possible to collect the
84 yearlong sea level records that are commonly employed to obtain reliable tidal constituents.
85 Approximately 269 km south of JBARS, there is a permanent tidal observation station named after its location on Cape Roberts
86 (ROBT), operated by Land Information New Zealand (LINZ) and recording at intervals since November 1990 (Figure 2). Five
87 minute interval sea level data have been collected at ROBT since November 2011 using Standard Piezometers (Model 4500,
88 GEOKON). Part of the 2017 record from this site was unavailable at the time of starting this research, so instead we chose as
89 our reference records the 2013 ROBT sea level data, a quality yearlong dataset with few missing points.

90 **2.2 Tidal characteristic analyses and descriptions**

91 Using the T_TIDE toolbox (Pawlowicz et al., 2002), we obtained the tidal harmonic constants of the 8 and 6 major tidal
92 constituents for ROBT and JBARS, respectively. In order to separate out the two major diurnal (K_1 versus P_1) and semi-diurnal
93 (S_2 versus K_2) tide constituents from the short term records at JBARS, we used the inference method. That is, we used inference
94 parameters (i.e., amplitude ratios and phase-lag differences) for each tidal constituent pair (K_1 versus P_1 ; and S_2 versus K_2)
95 derived from harmonic analysis of records from the nearby ROBT reference station. Analysis revealed that the dominant tides
96 in this area are diurnal (O_1 and K_1), with the second most important tides being semi-diurnal (M_2 and S_2) (Table 1). These four
97 tides were characterized by similar amplitudes between ROBT and JBARS: 21.1 and 19.6 cm for O_1 ; 20.5 and 16.3 cm for K_1 ;
98 5.3 and 6.7 cm for M_2 ; and 4.9 and 6.4 cm for S_2 . Note that the diurnal amplitudes were slightly larger at ROBT than at JBARS,
99 whereas the semi-diurnal amplitudes were slightly smaller at ROBT than at JBARS. Despite the relatively close distance (269
100 km) between ROBT and JBARS in tidal terms, the phase-lags showed slightly different values. The amplitude differences
101 result in slightly different tidal patterns as indicated by the two sites' tidal form factors (F). At ROBT F is 4.1 while at JBARS
102 F is 2.7: that is, ROBT has 'diurnal' type tides whereas JBARS has 'mixed, mainly diurnal' type tides.
103 Next we explored the characteristics of the four main tidal constituents around the entire Antarctic continent, using the
104 FES2014 database (Carrère et al., 2016). The horizontal distributions of the co-amplitudes and co-tides for K_1 , O_1 , M_2 and S_2
105 show that the diurnal tides rotate in an anticlockwise direction around Antarctica, with increasing co-amplitudes towards the
106 south, in particular, towards the Ronne and Ross ice shelves and hinterlands (Figure A1). In contrast, the M_2 and the S_2 tides
107 exhibit more complex patterns, with 5 and 7 amphidromic points respectively around Antarctica. Most of the semi-diurnal
108 tides rotate clockwise around their amphidromic points, except at one amphidromic point occurring $\sim 150^\circ$ W, where the S_2
109 tide rotates in an anticlockwise direction (Figure A2). The semi-diurnal co-amplitudes increase landwards in the Weddell Sea
110 but reduce across the entire Ross Sea quadrant, with relatively low semi-diurnal tide co-amplitudes (> 7 cm) in this area. These
111 FES2014 results reveal that the tides of the Ross Sea are very different to regimes elsewhere in Antarctica.

112 **3 Using the CTSM+TCC tidal prediction methodology in the Ross Sea**

113 In this study, we used the -CTSM+TCC method (Byun and Hart, 2015) to predict tidal heights for JBARS. This prediction
114 approach is based on the idea of being able to use comparisons between the tidal harmonic constants at a *temporary observation*
115 *station* (JBARS in our study) and at a nearby *reference tidal observation station* (ROBT in this case) that is situated in an area
116 with similar tidal characteristics to that of the temporary observation station. It requires three data sets: long-term (ideally ≥ 183
117 days duration, from anytime) sea level records (LH_R) from the reference station, plus concurrent 25 h sea level records from



118 both the temporary observation station (SH_o) and the reference station (SH_R). Note that Byun and Hart (2015) recommend
 119 using short-term data from periods with larger than average tidal ranges (e.g., in their situation these were spring tide periods
 120 due to their study site having a semi-diurnal tidal regime) to produce accurate CTSM+TCC predictions, with periods of below
 121 average tidal ranges (e.g., neap records) producing less accurate predictions. They also recommended the use of temporary
 122 records gathered during periods of calm weather, to minimize errors due to atmospheric influences.

123 A complicating factor in this study was that, for the 2017 summertime period when SH_o were recorded at JBARS, the ROBT
 124 records were poor quality, including multiple missing data up until 12 February 2017. As such we did not start with two quality,
 125 concurrent short-term observation records from our 2 stations. This issue was solved simply, using T_TIDE (Pawlowicz et al.,
 126 2002) to produce accurate 10 min interval 2017 yearlong tidal height predictions for ROBT, based on LH_R - that station's 2013
 127 yearlong and high quality record. In short, the LH_R dataset was harmonically analyzed to obtain harmonic constants for the
 128 tidal constituents. In turn, these harmonic constants were used to produce the modulated amplitudes ($A_{r\eta}^{(s)}(\tau)$) and phase-lags
 129 ($\varphi_{r\eta}^{(s)}(\tau)$) over the 2017 tidal prediction period. Note that the period of the modulated species amplitudes and phase-lags
 130 determine the tidal prediction period. Seventeen days of daily (25 h) data slices from the resulting 2017 tidal prediction data,
 131 overlapping temporally with the SH_o dataset, was then used as our SH_R dataset. Figure 3 shows the modulated amplitudes and
 132 phase-lags for the diurnal and semi-diurnal species, calculated from this SH_R summertime 2017 tidal prediction data.

133 Using the CTSM+TCC approach, tidal predictions for the temporary station ($\eta_o(\tau)$) were initially derived from reference tidal
 134 station predictions ($\eta_r(\tau)$) on the assumption that the tidal peculiarities between the two stations remain similar through time.
 135 This step is expressed in Byun and Hart (2015) as:

$$136 \quad \eta_r(\tau) = \sum_{s=1}^k A_{r\eta}^{(s)}(\tau) \cos(\omega_R^{(s)} t - \varphi_{r\eta}^{(s)}(\tau)) \quad (1)$$

137 with

$$138 \quad A_{r\eta}^{(s)}(\tau) = \sqrt{\sum_{i=1}^m [f(\tau)_i^{(s)} a_i^{(s)}]^2 + 2 \sum_{i < j}^m [f(\tau)_i^{(s)} a_i^{(s)}] [f(\tau)_j^{(s)} a_j^{(s)}] \cos\{(\omega_i^{(s)} - \omega_j^{(s)}) t + [V(t_0)_i^{(s)} + u(\tau)_i^{(s)} - g_i^{(s)}] - [V(t_0)_j^{(s)} + u(\tau)_j^{(s)} - g_j^{(s)}]\}} \quad (2)$$

139 and

$$140 \quad \varphi_{r\eta}^{(s)}(\tau) = \tan^{-1} \left(\frac{\sum_{i=1}^m a_i^{(s)} \sin[(\omega_i^{(s)} - \omega_R^{(s)}) t + V(t_0)_i^{(s)} + u(\tau)_i^{(s)} - g_i^{(s)}]}{\sum_{i=1}^m a_i^{(s)} \cos[(\omega_i^{(s)} - \omega_R^{(s)}) t + V(t_0)_i^{(s)} + u(\tau)_i^{(s)} - g_i^{(s)}]} \right) \quad (3)$$

141 where superscript s denotes the type of tidal species (e.g., 1 for diurnal species and 2 for semi-diurnal species), τ is time, m is
 142 the number of tidal constituents and $\omega_i^{(s)}$ and $\omega_R^{(s)}$ are the angular frequencies of each tidal constituent (subscripts i and j) and
 143 of representative tidal constituents (subscript R) for each species (e.g., K_1 and M_2 used as representative diurnal and semi-
 144 diurnal species, respectively). For each tidal constituent, $a_i^{(s)}$ and $g_i^{(s)}$ are the tidal harmonic amplitudes and phase-lags,
 145 $f(\tau)_i^{(s)}$ is the nodal factor, $u(\tau)_i^{(s)}$ is the nodal angle and $V(t_0)_i^{(s)}$ are the astronomical arguments. T_TIDE was used for tidal
 146 harmonic analysis as well as for calculation of the nodal factors, nodal angles and astronomical arguments for the representative
 147 species.

148 The amplitude ratio $\left(\frac{a_{o\eta}^{(s)}}{a_{r\eta}^{(s)}}\right)$ and phase-lag difference $(g_{o\eta}^{(s)} - g_{r\eta}^{(s)})$ of each representative tidal species between the temporary
 149 tidal observation station (subscript $o\eta$) and the reference station (subscript $r\eta$) were then calculated from tidal harmonic
 150 analysis of concurrent 25 h tidal records from both stations. In order to explore the best 25 h data window to use during this
 151 step, we sliced the 17 day SH_o and SH_R records (from 29 January to 14 February 2017) into individual 'daily' data slices, each
 152 starting at 00:00 and 25 h in duration. The 17 daily data slices from each station were harmonically analyzed (Figure 4) to
 153 calculate daily amplitude ratios $\left(\frac{a_{ou}^{(s)}}{a_{r\eta}^{(s)}}\right)$ and phase-lag differences $(g_{ou}^{(s)} - g_{r\eta}^{(s)})$ for the diurnal and semi-diurnal representative
 154 species (i.e., K_1 and M_2), as illustrated in Figure 5. The initial tidal predictions were then adjusted to represent those for the
 155 temporary station ($\eta_o(\tau)$) by substituting the above amplitude ratios and phase-lag differences between the temporary and
 156 reference stations into Eq. (1) as follows (Byun and Hart, 2015):



157 $\eta_o(\tau) = \sum_{s=1}^k A_{o\eta}^{(s)}(\tau) \cos(\omega_R^{(s)} t - \varphi_{o\eta}^{(s)}(\tau))$ (4)

158 with $A_{o\eta}^{(s)}(\tau) = A_{r\eta}^{(s)}(\tau) \left(\frac{a_{o\eta}^{(s)}}{a_{r\eta}^{(s)}} \right)$ and (5)

159 $\varphi_{o\eta}^{(s)}(\tau) = \varphi_{r\eta}^{(s)}(\tau) + g_{o\eta}^{(s)} - g_{r\eta}^{(s)}$ (6)

160 Substituting Eqs. (5) and (6) into Eq. (4), $\eta_o(\tau)$ can be expressed as:

161 $\eta_o(\tau) = \sum_{s=1}^k A_{r\eta}^{(s)}(\tau) \left(\frac{d_{o\eta}^{(s)}}{a_{r\eta}^{(s)}} \right) \cos[\omega_R^{(s)} t - (\varphi_{r\eta}^{(s)}(\tau) + g_{o\eta}^{(s)} - g_{r\eta}^{(s)})]$ (7)

162 where t_0 is the reference time, t is the time (t) elapsed since t_0 and $\tau = t_0 + t$.

163 In addition to the 2017 tidal height prediction experiments, we examined the capacity of the CTSM+TCC method to generate
164 tidal predictions for the period 29 December 2018 to 18 January 2019 (hereafter referred to in shorthand as ‘2019
165 summertime’), using the same 2017 input data (i.e. using data from Figure 3 and Figure 5 in Eq. (7)). This 2019 summertime
166 prediction period corresponds to the second tidal observation mission made to JBARS by KHOA surveyors.

167 4 Results

168 4.1 Tidal predictions

169 The CTSM+TCC experiments produced seventeen datasets, each comprising 17 day long, 10 min interval tidal height
170 predictions for JBARS, together with data on the ‘daily’ (25 h) amplitude ratios and phase-lag differences between our two
171 observation stations (JBARS and ROBT). In order to evaluate these CTSM+TCC results, each predicted tidal height dataset
172 was compared with the concurrent JBARS field observations via Root Mean Square Error (RMSE) and coefficient of
173 determination (R^2) statistics.

174 As illustrated in Figure 6, the RMSE and R^2 results varied in relation to the JBARS tidal ranges, with greater accuracy evident
175 in predictions made using data derived from 25 h periods where the tidal range was higher than average. In the JBARS ‘mixed,
176 mainly diurnal’ type tide area of the Ross Sea, during our 2017 observation period, greater than average tidal ranges
177 corresponded to the spring tide period when the moon was near its maximum (tropic) declination. RMSEs between
178 observations and predictions ranged from 4.26 cm to 20.56 cm while R^2 varied from 0 to 0.94 across the 17 ‘daily’ experiments.
179 Eleven of the experiments produced accurate results (i.e. excluding those based on 25 h input data derived from 31 January;
180 and 1 to 4 and 14 February records), with their RMSEs <5 cm and R^2 values >0.92. In contrast to the majority of successful
181 experiments, the experiment based on data derived from the ‘2 February’ 25 h data slice produced predictions with very high
182 RMSE (20.56 cm) and very low R^2 (0.00) values. Notably, the 2 February tides were characterized by the smallest tidal range
183 (11.95 cm) of the temporary JBARS record, during an equatorial tide period. In contrast, daily datasets from periods with
184 relatively high tidal ranges (>83.5 cm) produced predictions with RMSEs <5 cm and R^2 values >0.92. The maximum spring
185 tidal range occurred on 9 February: the data slice from this occasion produced predictions with a low (but not the lowest)
186 RMSE (4.81 cm). The predictions with the lowest RMSE (4.259 cm) and highest R^2 value (0.941) were produced using inputs
187 derived from 25 h data recorded one day earlier, on 8 February 2017.

188 As with the 2017 predictions, RMSEs between the 2019 summertime predictions and observations were lower when generated
189 using input data derived from 25 h data slices from the 2017 tropic – spring (as opposed to equatorial and/or neap) tide periods
190 (Figure 7). As in the earlier experiments, the 2019 summertime predictions made using input data derived from the 8 February
191 2017 (25 h) data slice produced the lowest RMSE (5.3 cm) and highest R^2 (0.913) values of the 2019 summertime experiments
192 (Figure 8).

193 These results demonstrate that the CTSM+TCC method can be successfully employed to predict tidal heights for JBARS for
194 any particular period, using 25 h observation records gathered from tropic or tropic-spring tide periods with relatively calm



195 weather, together with yearlong sea level observation or prediction records from the nearby reference station ROBT, despite
196 the two stations having slightly different types of tidal regime.

197 4.2 Determining the ideal short-term sea level observation period when using CTSM+TCC

198 The previous section verified that the CTSM+TCC method can be used to generate accurate tidal predictions based on 25 h
199 sea level records, from periods with higher than average tidal ranges, for a temporary station in a ‘mixed, mainly diurnal’
200 regime and a reference station in a ‘diurnal’ regime. The question arises as to how to determine the ideal day from which to
201 source the 25 h observation records in order to produce the most accurate tidal predictions.

202 For semi-diurnal or mixed, mainly semi-diurnal tidal regimes, we can estimate preferred temporary observation days based on
203 the moon’s phase, without reference to tide tables. That is, spring tides commonly occur just a day or two after the full and
204 new moon, which reoccurs at a period of 14.7653 days. The time lag between the full or new moon and the spring tide is called
205 the age of the tide (*AT*).

206 Similarly, in a ‘diurnal’ tide regime or a ‘mixed, mainly diurnal’ tide regime (Figure 6), the preferred temporary observation
207 days can be estimated based on the lunar declination, which varies at a period of 13.6608 days. That is, maximum range tropic
208 tide days can be estimated for JBARS based on the day of the Moon’s maximum and minimum declinations. The time between
209 the Moon’s semi-monthly maximum (and minimum) declinations and its maximum effect on tidal range, called the age of
210 diurnal inequality (*ADI*), is commonly 1 to 2 days.

211 As shown in Figure 9, the maximum and minimum Moon’s declinations during our 2 temporary summertime observation
212 periods occurred on 8 February 2017 (max) and on 6 January 2019 (min) respectively. The diurnal maximum tide tends to
213 occur ~1 day after the maximum declination, during one half of the tropic month and about 2 days after the minimum
214 declination during the other half of the tropic month.

215 4.3 Comparison of ROBT and JBARS tidal species characteristics

216 The CTSM+TCC tidal prediction method is based on the assumption that the tidal harmonic characteristics of each tidal species
217 are very similar between the temporary observation and reference stations. This is because the reference station tidal species’
218 CTSMs, derived from yearlong reference station sea level records or tidal harmonic analysis results, form the basis of the tidal
219 predictions for the temporary observation station. To test the validity of this assumption, we examined the phase-lag differences
220 of the 2 major diurnal (K_1 and O_1) and 2 major semi-diurnal tidal constituents (M_2 and S_2) using the age of diurnal inequality
221 (*ADI*) and the age of the tide (*AT*), calculated as:

$$222 \quad ADI \text{ (day)} = \left(\frac{\omega_{K_1} - \omega_{O_1}}{\omega_{K_1} + \omega_{O_1}} \right) / 24, \text{ and} \quad (7)$$

$$223 \quad AT \text{ (day)} = \left(\frac{\omega_{S_2} - \omega_{M_2}}{\omega_{S_2} + \omega_{M_2}} \right) / 24, \quad (8)$$

224 where ω_{K_1} (= 15.0410686° hr⁻¹), ω_{O_1} (= 13.9430356° hr⁻¹), ω_{M_2} (= 28.9841042° hr⁻¹) and ω_{S_2} (= 30.0000000° hr⁻¹) are the
225 angular speeds of the K_1 , O_1 , M_2 and S_2 tides, respectively.

226 Results revealed that the *ADI* are very similar, and there is <1 day *AT* difference, between the 2 stations: the *ADI* values were
227 0.57 versus 0.23 day, while the *AT* values were -2.30 versus -1.44 day, for ROBT versus JBARS (Table 1). These values
228 indicate that the tidal characteristics of the representative tidal constituents for each species between ROBT and JBARS are
229 very similar, in particular the dominant diurnal species. Hence the applicability and success of the CTSM+TCC method for
230 generating JBARS tidal predictions, using concurrent 25 h records from both stations and reference records from ROBT.



231 **5 Discussion**

232 **5.1 Fortnightly tide effects around Antarctica**

233 We have so far demonstrated that the CTSM+TCC approach can produce reasonably accurate tidal predictions (RMSE <5 cm,
234 $R^2 > 0.92$) for a new site in the Ross Sea, Antarctica, based on 25 h temporary observation records from periods with higher
235 than average tidal ranges, plus nearby reference station records.

236 Our results compare favourably with those of Han et al. (2013), who reviewed the tidal height prediction accuracy of 4 models
237 for Terra Nova Bay, Ross Sea: that is, TPXO7.1 developed by Egbert and Erofeeva (2002), FES2004 from Lyard et al (2006);
238 the Circum-Antarctic Tidal Solution (CATS2008a) from Padman et al. (2008), and the Ross Sea Height-Based Tidal Inverse
239 Model (Ross_Inv_2002) from Padman et al. (2003). Han et al. (2013) compared the model datasets to 11 days of February
240 2011 in situ sea level observations, corrected for inverse barometer effects, and considered model usefulness for investigating
241 tidal signals in satellite data from the Campbell Glacier tongue. The 4 models generated similar quality results to those
242 generated by the CTSM+TCC method in this study, with R^2 values varying between 0.876 and 0.907, and RMSEs ranging
243 from 3.6 and 4.1 cm.

244 However, as shown in Figure 8, our results appear to contain a changing bias in estimates occurring at fortnightly timescales,
245 with predictions slightly overestimating tides during the period from the equatorial to tropic tides (the ETT), and slightly
246 underestimating tides from the period between the -tropic to equatorial tides (the TET). This error pattern likely resulted from
247 our application of CTSM+TCC only considering 2 major tidal species, those representing diurnal and semi-diurnal
248 constituents, whilst ignoring long period tides.

249 In their GPS field measurement and modelling study of the Ronne Ice Shelf in the Weddell Sea, Rosier and Gudmundsson
250 (2018) found that ice shelf and ice stream horizontal flows are strongly modulated at a variety of tidal frequencies, with a
251 significant M_{sf} tide correlated signal occurring across their field site. Modelling without vertical tidal oscillations produced
252 horizontal ice flow rates almost 30% lower than observed. In an earlier Synthetic Aperture Radar (SAR) interferometry and
253 tide model comparison study of the Ronne and Filchner Ice Shelves, Rignot et al. (2000) found that eight ‘major’ tidal
254 constituents (M_2 , S_2 , K_2 , N_2 , O_1 , K_1 , Q_1 , and $2N_2$) plus an additional 18 ‘minor’ constituents measurably influenced patterns
255 of ice flexure and motion. The authors of both of these papers recommend the inclusion of both major and minor tidal
256 constituents, including long period tides, for successful ice flow and ice-ocean front modelling.

257 Long period tides cycle across timeframes including 18.61 y, seasons, months and fortnights (Woodworth, 2012). Table 2
258 summarizes the characteristics of 6 long-period tides (S_a , S_{sa} , M_{sm} , M_m , M_f , M_{sf}) at the ROBT station, derived from tidal
259 harmonic analysis of yearlong (2013) in situ records. Comparisons between Tables 1 and 2 reveal that the S_a amplitude (5.8
260 cm) was similar to that of the M_2 (5.3 cm), the amplitudes of the M_m and M_f tides were >50 % of the M_2 (≥ 2.7 cm), while the
261 S_{sa} and M_{sm} amplitudes were all minor (≤ 0.4 cm). While the 2013 S_a amplitude was equivalent to that of the M_2 , inter-annual
262 variation in the S_a harmonic constant is large (1.2 cm to 9.1 cm for amplitude; 75° to 131° for phase-lag, Table 3). This is
263 because the S_a constituent comprises both astronomical and seasonal components (Pugh, 1987). Hence our focus here on the
264 error bias between the ETT and TET periods.

265 In order to verify the main cause of the apparent fortnightly prediction biases, in particular that found in the 2019 summertime
266 results (Figure 8b), we examined the effects of two fortnightly period tidal constituents (M_f and M_{sf}) at ROBT. Three 2019
267 summertime tidal prediction experiments were conducted: 1) *Run1* excluding all long-period tides (i.e. those in Table 2); 2)
268 *Run2* incorporating the M_f alone; 3) *Run3* incorporating the M_f and the M_{sf} alone.

269 Results revealed that exclusion of the M_f tide (2.7 cm amplitude) alone can produce ETT and TET prediction biases (Figure
270 10a), with exclusion of the M_{sf} tide (1.2 cm amplitude) intensifying the biases (Figure 10b). Thus, consideration of additional,
271 fortnightly timescale tidal constituents in predictions is our recommended next step for improving tidal prediction accuracies
272 for JBARS.



273 **5.2 Decadal scale tidal variations around Antarctica**

274 Tidal regime characteristics in the seas surrounding Antarctica mostly fall into three of the four daily form factor types, as
275 revealed by FES2014 model data. Figure 11 shows there are areas of ‘diurnal’ (DD); ‘mixed, mainly diurnal’ (MD); and
276 ‘mixed, mainly semi-diurnal’ (MS) forms. Only in a small area half-way along the Weddell Sea coast of Antarctic Peninsula
277 do tides exhibit a ‘semi-diurnal’ form. Strong ‘diurnal’ tides ($F>3$) predominate in the Ross Sea area of West Antarctica,
278 around to the Amundsen Sea. In addition, a small area near Prydz Bay in East Antarctica exhibits diurnal and mixed mainly
279 diurnal tides. The rest of the seas surrounding Antarctica, including the Weddell Sea, are predominantly characterized by
280 ‘mixed, mainly semi-diurnal’ tides.

281 Tides around the Weddell Sea coast are significantly amplified due to shoreline shape and bathymetric shoaling effects, with
282 the increase in semi-diurnal amplitudes ($a_{M_2} + a_{S_2}$) being more pronounced than those of the diurnal tides ($a_{K_1} + a_{O_1}$). Tidal
283 ranges >2 m are largely confined to the Weddell Sea region, with the exception of the area surrounding the M_2 tide
284 amphidromic point at the head of the Weddell Sea embayment, where relatively large ‘mixed, mainly semi-diurnal’ tides occur
285 thanks to the pronounced M_2 and S_2 amplitudes there.

286 The contrasting tidal environments of the Weddell and Ross Seas feature different tidal dynamics and, thus, different tidal
287 influences on their environments, across the full 18.61 y tidal cycle. Accurate (cm scale) quantification of the tidal cycle
288 patterns resulting from these different regimes are essential for calculating ice-sheet motion near Antarctica’s different ocean
289 margins, based on the subtraction of ice flexure and tidal elevation changes from land ice elevation measurements (Wild et al.,
290 2019). Such studies contribute to our understanding of global climate models, providing estimates of ice sheet and glacier
291 flows to the sea.

292 A question arises as to how much the Weddell and Ross Sea tidal form differences can be explained by tidal height changes.
293 To answer this, we explored variation in nodal modulation correction factors (nodal factors and nodal angles) over an 18.61 y
294 cycle. Daily nodal modulation correction factor values for the 3 major lunar tide constituents (K_1 , O_1 and M_2) were estimated
295 for JBARS over the 20 y period 2011 to 2030, as illustrated in Figure 12. Interestingly the diurnal, O_1 tide variations in nodal
296 modulation correction factors were the largest (nodal factor range = 0.3833; nodal angle range = 22.59°), with those of the K_1
297 tide being second largest (nodal factor range = 0.2320; nodal angle range = 17.86°). In comparison, those of the semi-diurnal,
298 M_2 tide were relatively small (nodal factor range = 0.0754; nodal angle range = 4.39°).

299 These nodal modulation correction factor variations have different implications for the Weddell and Ross Seas due to their
300 differing tidal regimes. The resulting variations in tidal height are less pronounced in the semi-diurnal Weddell Sea, while the
301 diurnal regime of the Ross Sea experiences large tidal range variations across 18.61 y cycles due to the influence of diurnal
302 nodal factor variation. Of note, variations in the nodal factors of the O_1 and K_1 tides are out of phase with that of the M_2 tide
303 (Figure 12a). Variations in the nodal angle of the K_1 tide is in phase with that of the M_2 tide but out of phase with that of the
304 O_1 tide (Figure 12b).

305 **6 Conclusions**

306 This paper has demonstrated the usefulness of the CTSM+TCC method for tidal prediction in extreme environments, where
307 long-term tidal station installations are difficult, using the Ross Sea in Antarctica for our case study. Here CTSM+TCC
308 methods can be employed for accurate tidal height predictions for a temporary tidal observation station using short-term (≥ 25
309 h) sea level records from this site, plus long-term (1 y) tidal records from a nearby reference tidal station. Essentially the
310 temporary and reference station sites must share similarities in their main tidal constituent and tidal species characteristics for
311 CTSM+TCC to produce accurate results.

312 Using this approach, an initial tidal prediction time series is generated for the temporary station using CTSM and the reference
313 station long-term records. The temporary station predicted time series can then be adjusted via TCC of each tidal species,



314 based on comparisons between the short-term temporary station observation record and its corresponding modelled
315 predictions, leading to improved accuracy in the tidal predictions.
316 This paper has further demonstrated that the CTSM+TCC approach can be employed successfully in the absence of concurrent
317 short-term (25 h) records from the reference station, since a tidal harmonic prediction program can be used to produce a
318 synthetic short-term record for the reference station based on a quality long-term record from that site.
319 The proper consideration of long-period tides in the CTSM+TCC approach remains a challenge, as outlined in this study, with
320 the solutions to this issue likely to improve the accuracy of CTSM+TCC tidal predictions even further. However, this study
321 demonstrates that the method can already produce tidal predictions of sufficient accuracy to aid scientists studying important
322 issues such as the rate and role of ice loss along polar coastlines.

323 **Code Availability**

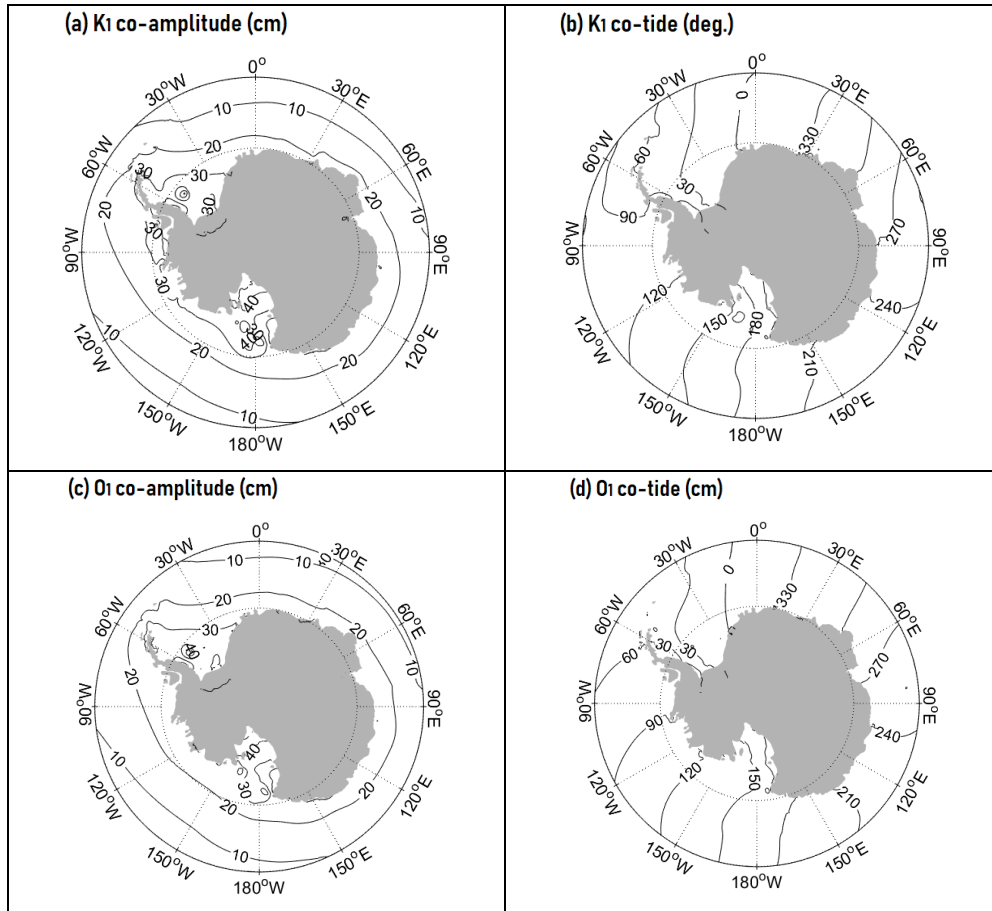
324 The T_TIDE based CTSM code is available from https://au.mathworks.com/matlabcentral/fileexchange/73764-ctsm_t_tide.

325 **Data Availability**

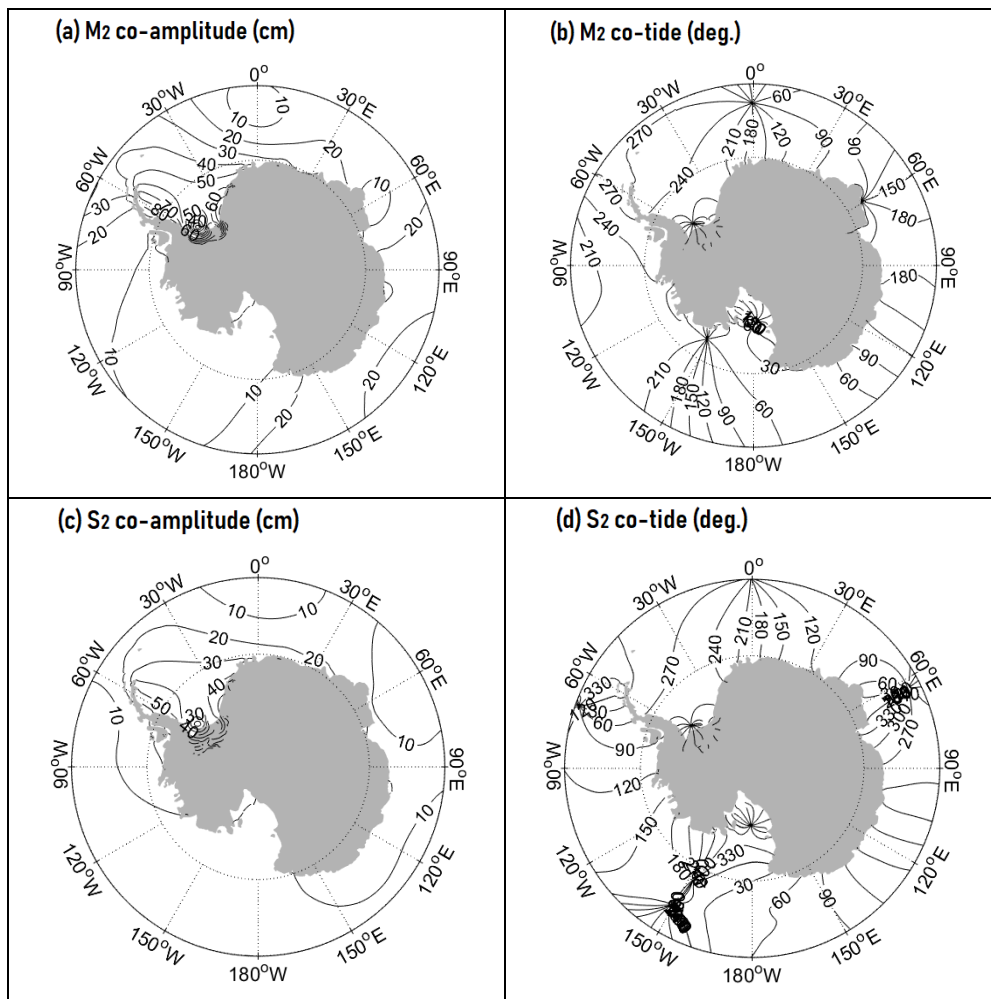
326 The sea level data used in this paper are available from LINZ (2019) for selected ROBT records, with the remaining ROBT
327 records available by email application (customersupport@linz.govt.nz); and the JBARS records used are available on request
328 from KHOA (infokhoa@korea.kr). Details of the FES2014 tide model database are found in Carrère et al. (2016) and via
329 <https://www.aviso.altimetry.fr/en/data/products/auxiliary-products/global-tide-fes.html>.



330 Appendix 1



331 Figure A1. Horizontal distributions of the K_1 and O_1 constituents' co-amplitudes (a, c) and co-tides (b, d) around Antarctica.



332 Figure A2. Horizontal distributions of the M₂ and S₂ constituents' co-amplitudes (a, c) and co-tides (b, d) around Antarctica.



333 **Author contribution**

334 D-SB conceived of the tidal prediction idea behind this paper, and wrote the results sections. Both authors worked on initial
335 and final versions of the full manuscript.

336 **Competing interests**

337 The authors declare that the research was conducted in the absence of any commercial or financial relationships that could be
338 construed as a potential conflict of interest.

339

340 **Acknowledgements**

341 We are grateful to Land Information New Zealand (LINZ) and the Korea Hydrographic and Oceanographic Agency (KHOA)
342 for supplying the tidal data used in this research. A special thank you to Glen Rowe from LINZ for sharing his extensive
343 knowledge of the Cape Roberts sea level gauge site and its records. Further, we gratefully thank Ms. Hyowon Kim at KHOA
344 for her kind assistance with drafting figures.

345 **References**

- 346 Byun, D.-S. and Hart, D. E.: Predicting tidal heights for new locations using 25h of in situ sea level observations plus reference
347 site records: A complete tidal species modulation with tidal constant corrections, *J. Atmos. Ocean. Tech.*, 32, 350–371, 2015.
348 Carrère L., Lyard, F., Cancet, M., Guillot, A. and Picot, N.: FES 2014, a new tidal model - validation results and perspectives
349 for improvements, Presentation to ESA Living Planet Conference, Prague, 2016.
350 Codiga, D. L.: Unified Tidal Analysis and Prediction Using the UTide Matlab Functions, Technical report 2011-01, Graduate
351 School of Oceanography, University of Rhode Island, 2011.
352 Egbert, G. and Erofeeva, S.: Efficient Inverse Modeling of Barotropic Ocean Tides, *J. Atmos. Ocean. Tech.*, 19, 183–204,
353 [https://doi.org/10.1175/1520-0426\(2002\)019<0183:EIMOOB>2.0.CO;2](https://doi.org/10.1175/1520-0426(2002)019<0183:EIMOOB>2.0.CO;2), 2002.
354 Foreman, M. G. G.: Manual for Tidal Heights Analysis and Prediction, Pacific Marine Science Report, 77-10, 1977.
355 Han, H. and Lee, H.: Glacial and tidal strain of landfast sea ice in Terra Nova Bay, East Antarctica, observed by interferometric
356 SAR techniques, *Remote Sens. Environ.*, 209, 41–51, <https://doi.org/10.1016/j.rse.2018.02.033>, 2018.
357 Han, H., Lee, J., and Lee, H.: Accuracy assessment of tide models in Terra Nova Bay, East Antarctica, for glaciological studies
358 of DDInSAR technique, *Korean Journal of Remote Sensing*, 29, 375–387, 2013.
359 Han, S. C., Shum, C. K., and Matsumoto, K.: GRACE observations of M2 and S2 ocean tides underneath the Filchner-Ronne
360 and Larsen ice shelves, Antarctica, *Geophys. Res. Lett.*, 32, L20311, <https://doi.org/10.1029/2005GL024296>, 2005.
361 Jourdain, N. C., Molines, J.-M., Le Sommer, J., Mathiot, P., Chanut, J., de Lavergne, C., and Madec, G.: Simulating or
362 prescribing the influence of tides on the Amundsen Sea ice shelves, *Ocean Model.*, 133, 44–55,
363 <https://doi.org/10.1016/j.ocemod.2018.11.001>, 2018.
364 LINZ, Land Information New Zealand: Sea level data downloads, [http://www.linz.govt.nz/sea/tides/sea-level-](http://www.linz.govt.nz/sea/tides/sea-level-data/sea-level-)
365 data-downloads, last access 2019.
366 Lyard, F., Lefevre, F., Letellier, T., and Francis, O.: Modelling the global ocean tides: modern insights from FES2004, *Ocean*
367 *Dynam.*, 56, 394–415, 2006.



- 368 Padman, L., Erofeeva, S., and Fricker, H.: Improving Antarctic tide models by assimilation of ICESat laser altimetry over ice
369 shelves, *Geophys. Res. Lett.*, 35, L22504, <https://doi.org/10.1029/2008GL035592>, 2008.
- 370 Padman, L., Erofeeva, S., and Joughin, I.: Tides of the Ross Sea and Ross Ice Shelf cavity, *Antarct. Sci.*, 15, 31–40,
371 <https://doi.org/10.1017/S0954102003001032>, 2003.
- 372 Padman, L., Fricker, H., Coleman, R., Howard, S., and Erofeeva, L.: A new tide model for the Antarctic ice shelves and seas,
373 *Ann. Glaciol.*, 34, 247–254, <https://doi.org/10.3189/172756402781817752>, 2002.
- 374 Padman, L., Siegfried, M., and Fricker, H.: Ocean Tide Influences on the Antarctic and Greenland Ice Sheets, *Rev. Geophys.*,
375 56, 142–184, <https://doi.org/10.1002/2016RG000546>, 2018.
- 376 Pawlowicz, R., Beardsley, B., and Lentz, S.: Classical tidal harmonic analysis including error estimates in MATLAB using
377 *T_TIDE*, *Comput. Geosci.*, 28(8), 929–937, doi:10.1016/S0098-3004(02)00013-4, 2002.
- 378 Pugh, D. T.: *Tides, Surges and Mean Sea-Level: A Handbook for Engineers and Scientists*, Wiley, Chichester, United
379 Kingdom, 1987.
- 380 Rignot, E., Padman, L., MacAyeal, D., and Schmeltz, M.: Observation of ocean tides below the Filchner and Ronne Ice
381 Shelves, Antarctica, using synthetic aperture radar interferometry: Comparison with tide model predictions, *J. Geophys. Res.-*
382 *Oceans*, 105, 19615–19630, <https://doi.org/10.1029/1999JC000011>, 2000.
- 383 Rosier, S. H. R. and Gudmundsson, G. H.: Tidal bending of ice shelves as a mechanism for large-scale temporal variations in
384 ice flow, *The Cryosphere*, 12, 1699–1713, <https://doi.org/10.5194/tc-12-1699-2018>, 2018.
- 385 Wild, C.T., Marsh, O.J., and Rack, W.: Differential interferometric synthetic aperture radar for tide modelling in Antarctic ice-
386 shelf grounding zones, *The Cryosphere*, 13(12), 3171–3191, doi.org/10.5194/tc-13-3171-2019, 2019.
- 387 Woodworth, P. L.: A note on the nodal tide in sea level records, *J. Coastal Res.*, 28(2), 316–323, 2012.
- 388



389 **Table 1.** Major tidal harmonic results for diurnal and semi-diurnal constituents from harmonic analyses of yearlong (2013) sea level
390 observations recorded at Cape Roberts (ROBT), and from 17 day sea level observations (29 January to 15 February 2017) and 20.54
391 day sea level observations (29 December 2018 to 18 January 2019) recorded at the Jang Bogo Antarctic Research Station (JBARS),
392 in Antarctica. For the JBARS tidal harmonic analyses, the inference method was applied to separate out the K₁ (S₂) and P₁ (K₂) tidal
393 constituents, using inference parameters estimated from the ROBT 2013 harmonic analysis. Phase-lags are referenced to 0°,
394 Greenwich.

Tidal constituents		ROBT (2013)		JBARS (2017)		JBARS (2019)		Note
		369 days	17 days	21 days				
		$a_{r\eta}$ (cm)	$g_{r\eta}$ (°)	$a_{o\eta}$ (cm)	$g_{o\eta}$ (°)	$a_{o\eta}$ (cm)	$g_{o\eta}$ (°)	
Diurnal	O ₁	21.1	202	19.6	208	16.0	208	ROBT: Diurnal tides ($F=4.1$) $ADI=0.57$ day $AT=-2.30$ days
	K ₁	20.5	217	16.3	214	14.9	216	
	P ₁	6.6	215	5.2	213	4.8	214	
	Q ₁	4.4	190	-	-	-	-	
Semi-diurnal	M ₂	5.3	5	6.7	4	6.3	34	JBARS: Mixed, mainly diurnal tides ($F=2.7$) $ADI=0.23$ day $AT=-1.44$ days
	S ₂	4.9	309	6.4	329	6.6	324	
	N ₂	3.8	255	-	-	-	-	
	K ₂	1.8	315	2.4	333	2.4	328	

395 Note that ADI and AT denote the age of diurnal inequality and the age of the tide.



396 **Table 2. Harmonic constants for 6 long-period tidal constituents, derived from harmonic analyses of yearlong observations (2013)**
397 measured at the Cape Roberts sea level gauge (ROBT)

Constituent		Period (day)	Angular speed (° hr ⁻¹)	Amplitude (cm)	Phase-lag (°)
Solar annual	S_a	365.24	0.0410686	5.8	75
Solar semi-annual	S_{sa}	182.62	0.0821373	0.1	352
Lunar monthly	M_{sm}	31.81	0.4715280	0.4	57
	M_m	27.55	0.5443747	2.9	139
Lunar fortnightly	M_{sf}	14.77	1.0158958	1.2	281
	M_f	13.66	1.0980331	2.7	153

398 Phase-lags are referenced to 0°, Greenwich.



399 **Table 3. Harmonic constants for the S_a constituent derived from harmonic analyses of 4 separate yearlong observation records**
400 **(2008; 2011; 2012; 2013) measured at the Cape Roberts sea level gauge (ROBT)**

Year	Amplitude (cm)	Phase-lag ($^{\circ}$)
2008	9.1	131
2011	1.2	90
2012	3.4	108
2013	5.8	75

401 Phase-lags are referenced to 0° , Greenwich.



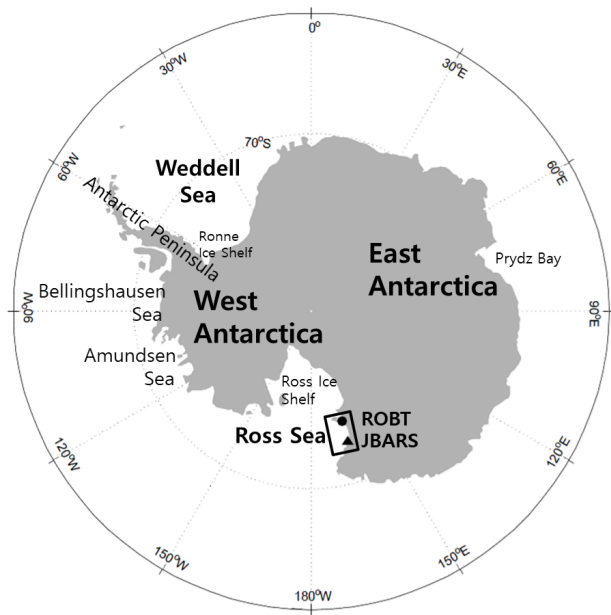
402

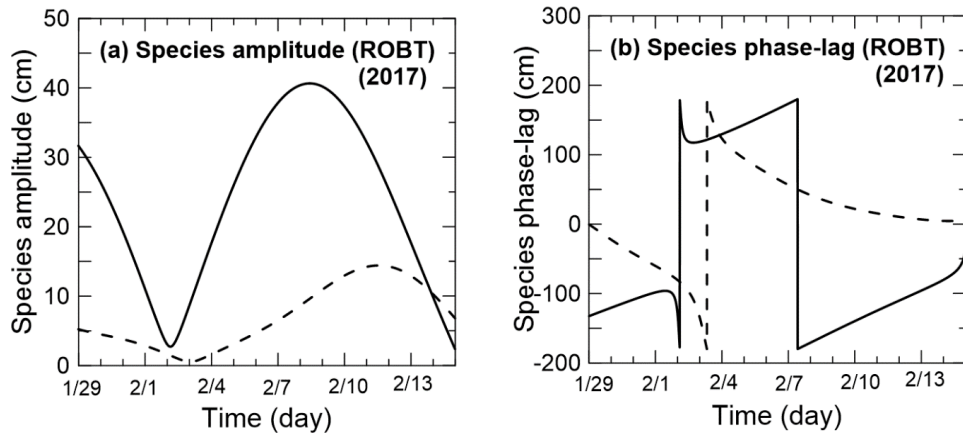
403 **Figure 1. Drifting ice, including icebergs and mobile sea ice, around the Jang Bogo Antarctic Research Station (JBARS).**



404

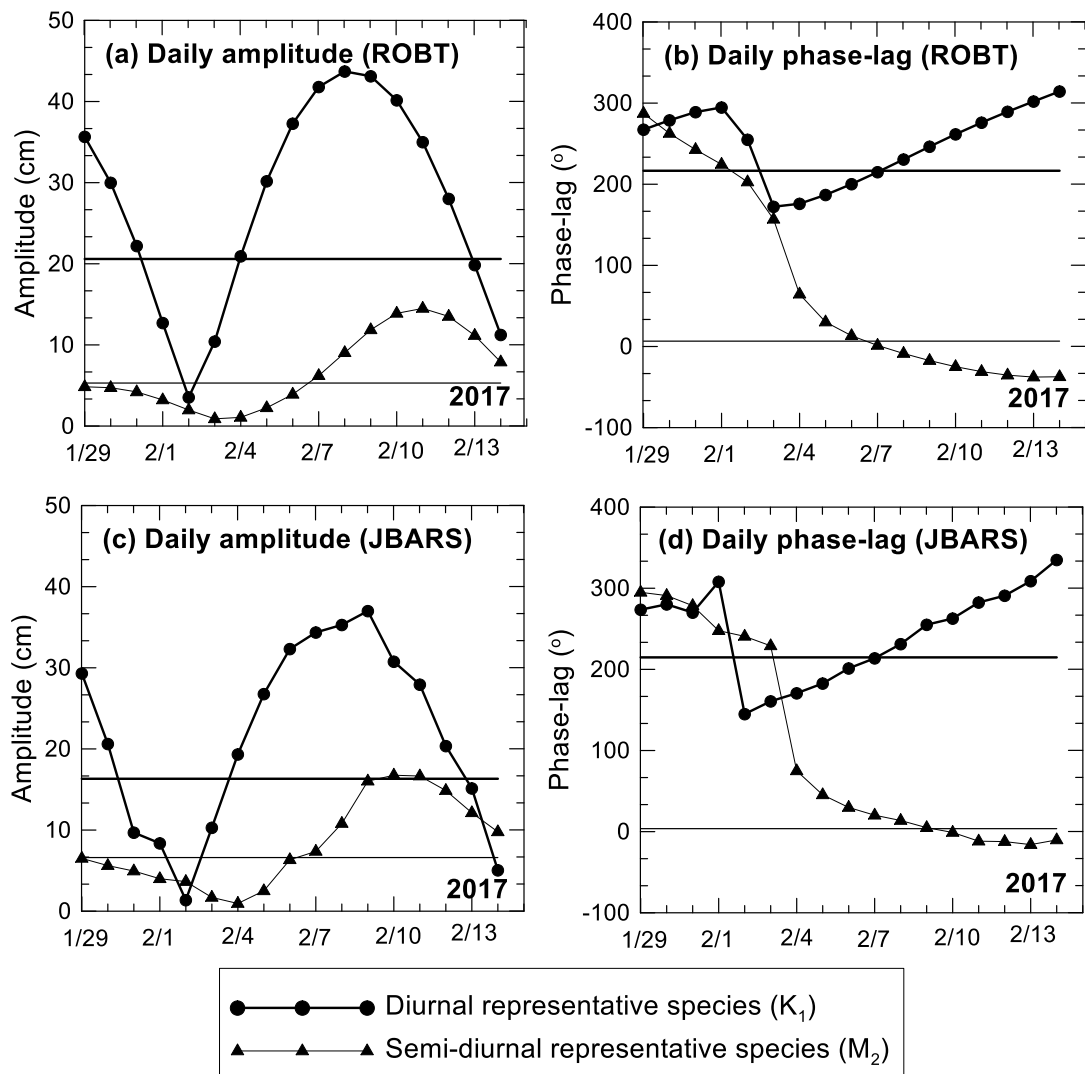
405 **Figure 2.** Map showing locations of two tidal observation stations in the Ross Sea of Antarctica: Jang Bogo Antarctic Research
406 Station (JBARS, ▲) and Cape Roberts (ROBT, ●).





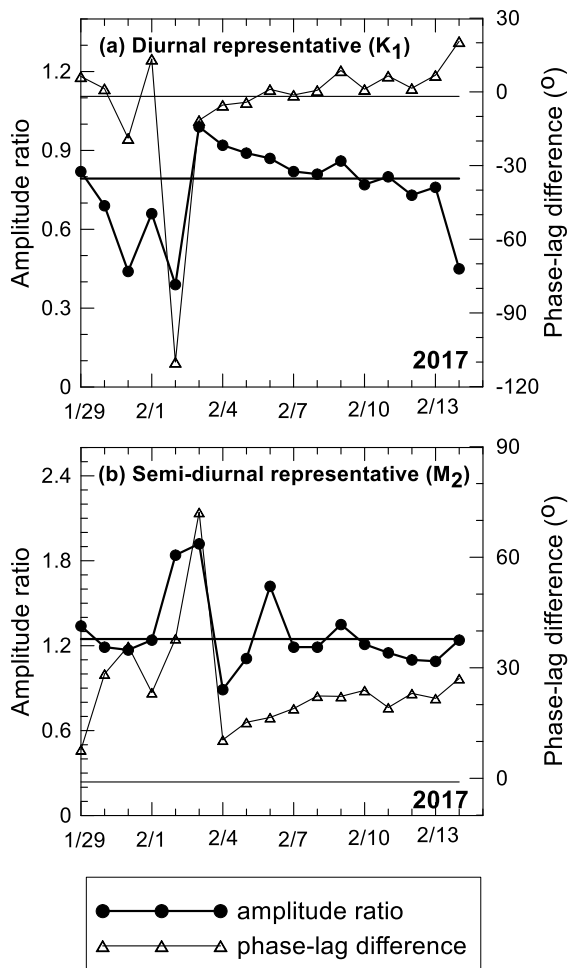
407

408 **Figure 3.** Seventeen day time series (29 January to 14 February 2017) of the modulated tidal (a) species amplitudes and (b) phase-
409 lags for the diurnal (solid lines) and semi-diurnal tides (dashed lines), estimated from the 2017 Cape Roberts (ROBT) tidal prediction
410 data.



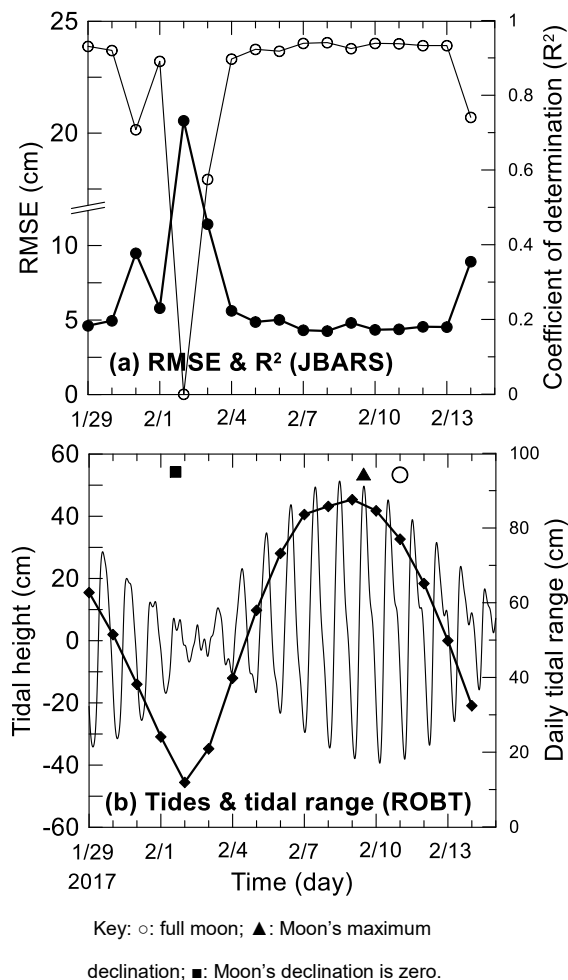
411

412 Figure 4. Daily amplitudes and phase-lags of the K_1 tide (diurnal representative species)
 413 and M_2 tide (semi-diurnal representative species) at ROBT and JBARS, estimated from 25 h daily data slices of the 17 day ROBT tidal predictions and
 414 JBARS sea level observations, 29 January to 14 February 2017. Thick solid (K_1) and thin gray (M_2) lines in each panel indicate the amplitude and
 415 phase-lag derived from results of the 369 day 2013 ROBT and 17 day 2017 summertime JBARS sea level record harmonic analyses,
 416 respectively.



417

418 **Figure 5.** The daily amplitude ratios and phase-lag differences of the (a) diurnal (K_1) and (b) semi-diurnal (M_2) species representative
419 tidal constituents, calculated harmonically from JBARS sea level data and ROBT predicted tidal height data, using harmonic inputs
420 derived from analysis of ‘daily’ (25 h) data slices. Thick solid and dashed lines in each panel indicate the amplitude ratio and phase-
421 lag differences, respectively for each tide, derived from harmonic analysis of the 17 day 2017 JBARS sea level data.



422

423

424

425 **Figure 6.** (a) Time series of Root Mean Square Errors (RMSE, thick line with ●) and coefficients of determination (R^2 , thin line with ○) between JBARS 10 min interval sea level observations (29 January to 15 February 2017) and the CTSM+TCC prediction datasets
426 generated for this site using harmonic analysis results from the daily (25 h) sea level data slices from JBARS plus concurrent daily
427 (25 h) tidal prediction slices and harmonic analysis results from ROBT station's yearlong (2017) tidal predictions. (b) Time series of
428 predicted 2017 tidal heights (thin line) and daily tidal ranges (thick line with ○) for ROBT, based on harmonic analysis of this
429 station's 2013, 5 min interval sea level records, plus an indication of the moon's phase and declination.
430

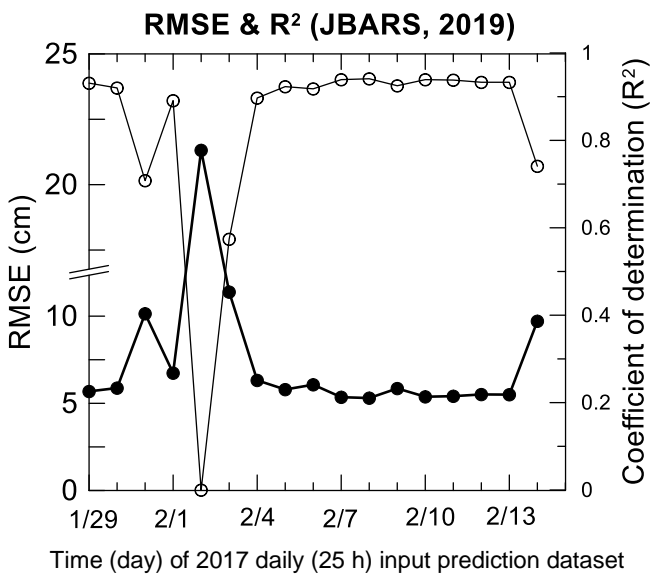
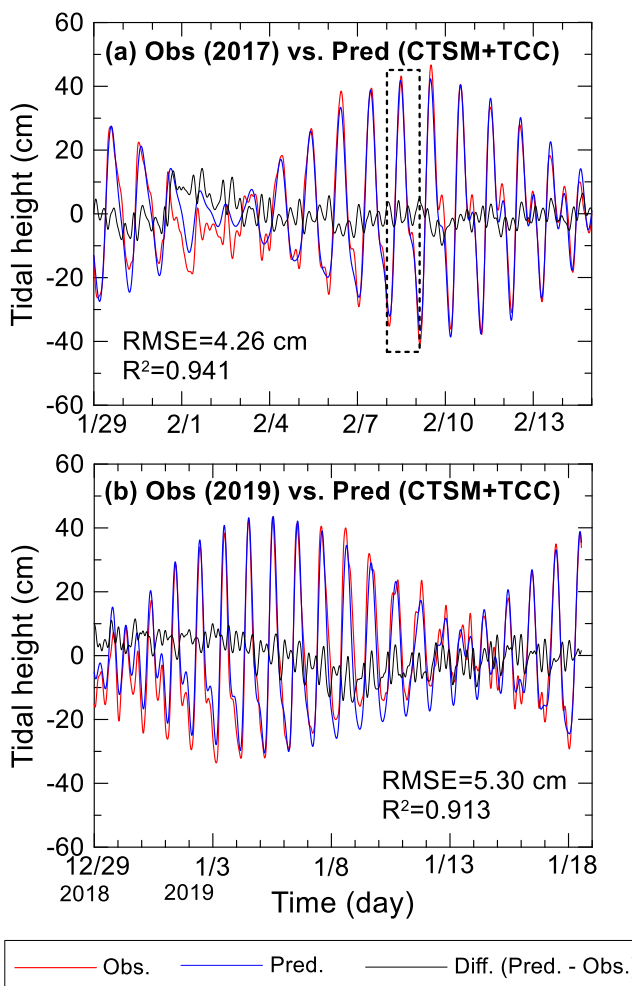
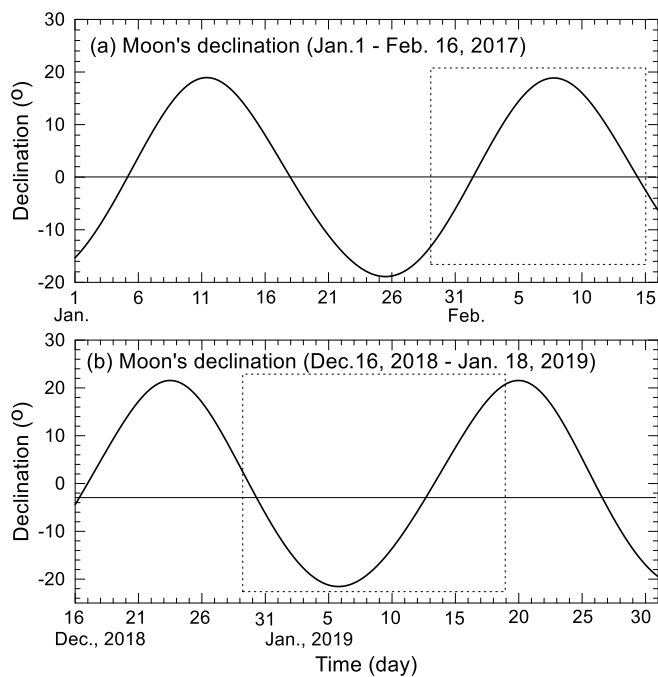


Figure 7. Time series of Root Mean Square Errors (RMSE, thick line with ●) and coefficients of determination (R^2 , thin line with ○) between JBARS 10 min interval sea level observations (29 December 2018 to 18 January 2019) and the CTSM+TCC prediction datasets generated for this site using harmonic analysis results from daily (25 h) summertime 2017 sea level data slices from JBARS plus concurrent daily (25 h) tidal prediction slices and harmonic analysis results from ROBT station's yearlong (2017) tidal predictions.



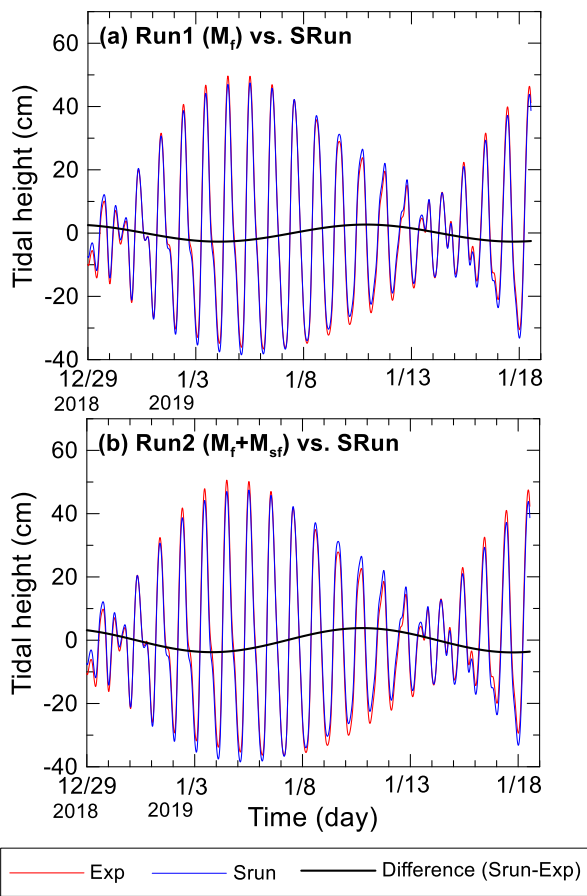
438

439 Figure 8. Time series of JBARS sea level observations, predicted tidal heights, and sea level residuals (i.e. predictions minus
440 observations) from (a) 29 January to 15 February 2017 and (b) 29 December 2018 to 18 January 2019. The JBARS predictions were
441 generated using CSTM+TCC, with a daily (25 h) slice of local sea level observations from 8 February 2017 (dashed box in (a)), plus
442 concurrent predictions and yearlong (2017), 5 min interval ROBT tidal predictions.



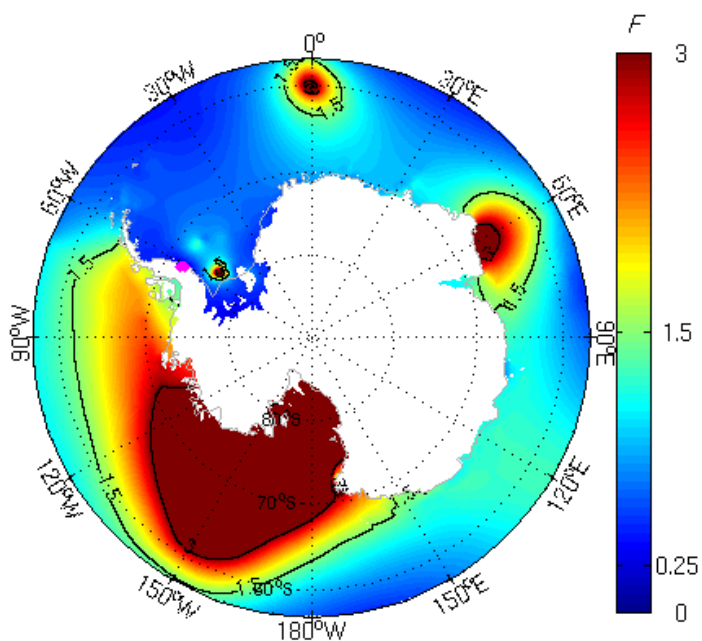
443

444 **Figure 9.** Time series of the Moon's declination, estimated at daily intervals for two observation periods: (a) 1 January to 15 February
445 2017; and (b) 16 December 2018 to 30 January 2019. Dashed boxes indicate the sea level observation windows examined in this
446 study.



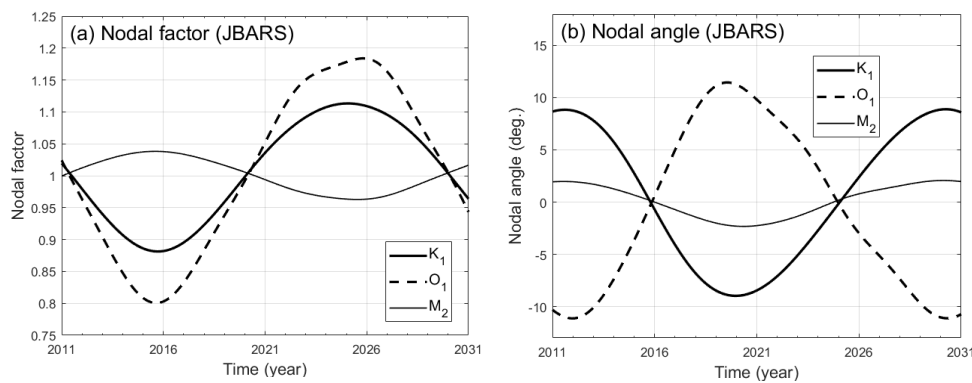
447

448 **Figure 10.** Time series of ROBT tidal predictions (a) made without long-period constituents ('SRun', i.e. excluding the constituents
449 listed in Table 2) versus with the M_f tide ('Exp1'); and (b) time series of ROBT tidal predictions made ('SRun') without the long-
450 period constituents versus ('Exp2') with the M_{sf} tide. All predictions were generated based on tidal harmonic analysis results from
451 the yearlong (2013) ROBT sea level records.



452

453 **Figure 11. Horizontal distribution of tidal form factor (F) values around Antarctica. Note the magenta area on the Antarctic**
454 **Peninsula's Weddell Sea coast denotes the only area of semi-diurnal tides ($F<0.25$) in the Antarctic region.**



455 **Figure 12.** Variation in nodal factors and nodal angles for the three main lunar tidal constituents (K₁, O₁ and M₂) over a 20 year
456 period from 2011 to 2030 at Jang Bogo Antarctic Research Station (JBARS), estimated at daily intervals from the t_vuf.m program
457 of T_Tide (Pawlowicz et al., 2002).